Growth and morphology of metal particles on MgO/Mo(001): A comparative STM and diffraction study

Stefania Benedetti,[1] Philipp Myrach,[2] Alessandro di Bona,[1] Sergio Valeri,[1,3] Niklas Nilius,[2,*] and Hans-Joachim Freund[2]

[1]*Consiglio Nazionale delle Ricerche, Istituto Nanoscienze, Centro S3, Via G. Campi 213/a, 41100 Modena, Italy*

[2]*Fritz-Haber-Institut der Max-Planck-Gesellschaft, Faradayweg 4-6, D-14195 Berlin, Germany*

[3]*Dipartimento di Fisica, Università di Modena e Reggio Emilia, Via G. Campi 213/a, 41100 Modena, Italy*

Using scanning tunnelling microscopy and photoelectron diffraction, we have analyzed the nucleation and growth behavior of simple (Mg and Ca), transition (Ni and Fe), and noble metals (Ag and Au) on MgO films grown on Mo(001). With the exception of gold, the particles develop interface planes that are in registry with the surface-oxygen lattice of the MgO(001). To achieve this commensurability, the particles expose facets that differ from the low-energy surfaces of the respective metals and adopt crystallographic structures that are unknown in the bulk materials. This peculiar growth behavior demonstrates the importance of interfacial interactions between the metal deposits and the MgO film, despite the inert nature of the oxide support. The observed equilibrium shapes of the particles have been analyzed with a simple growth model that includes the interfacial interactions, the surface energies, and the elastic distortion of the particle lattice to reach commensurability with the MgO(001). Experimental particle densities have been explained with a scheme that considers formation of metal cations at certain MgO defects to be the initial nucleation step. Although the model is in reasonable agreement with the experimental results for most metals, it fails for gold. We relate this deviation to the large tendency of gold to charge up negatively on MgO thin films, in correspondence with earlier experimental and theoretical work.

I. INTRODUCTION

Supported metal particles play a pivotal role as chemically active species in heterogeneous catalysis.[1] The chemical identity of the particles, which are usually made of transition metals, is the most decisive factor for determining the performance of the catalyst. However, it is by far not the only factor, as also the interplay between the metal aggregates and the underlying oxide support contributes greatly to the properties of the system.[2,3] Consequently, only certain combinations of admetal and oxide support give rise to chemical activity, and among such systems only those that are thermodynamically stable, can be fabricated at an industrial scale and are reasonably priced will finally make a functional catalyst.[1]

The importance of mutual interactions between metal deposits and the underlying oxide support was realized long ago, and the exploration of this interplay has therefore been in the focus of catalysis research for several decades.[4–7] Especially with the advent of surface science, the understanding of the various interaction schemes has greatly improved, leading to a rather complex and multifaceted picture of metal-oxide interactions. Only some key points of this relationship shall be sketched here.

First of all, the nucleation and growth of metal particles is restricted to distinct regions on the oxide surface, mostly to defects and low-coordinated lattice sites. Although the corresponding surface areas could be visualized already in the 1970s by exploiting decoration effects in electron microscopy,[8] it was the development of powerful theoretical methods that yielded a mechanistic insight into the binding behavior of adatoms to oxide defects.[9,10] Verification of the theoretical models has been achieved even more recently by scanning probe techniques, which rendered an atomic-scale characterization of oxide defects[11–13] and their adsorption characteristics

possible.[14] The nucleation phase determines various electronic and chemical properties of the metal-oxide system, as the process of anchoring a metal cluster is often accompanied by a charge exchange with the oxide support.[9,10,15]

Second, the substrate imposes large effects on the size and shape of the growing particles.[16,17] Whereas the particle size depends mainly on the density of suitable nucleation sites, and hence on surface properties, the particle shape is governed by the strength of the interfacial adhesion. The relationship between the equilibrium shape of a deposit and metal-oxide interactions was put on theoretical grounds already long ago, for instance in the Wulff model[18] and the more general Young-Dupré approach.[19] The shape of supported particles is correlated with their chemical performance in various ways.[20] It determines which particle facets are primarily exposed and controls the exchange of adsorbates between those planes. The shape also affects the electronic structure of the deposits, for instance by inducing distinct quantum-well and surface states in the spatially confined systems.[21,22] All these effects have an influence on the reactivity pattern of supported metal catalysts.

To a certain extent, metal-support interactions even influence the chemical identity of the adparticles, which naturally interferes with their chemical performance. This becomes evident when considering the deposition of a highly oxidizable metal onto a reducible oxide. In this case, substrate oxygen may dissolve in the particle, changing its oxidation state, electron count, and even lattice parameter.[23,24] The impact of a substrate-mediated oxidation of adparticles on their chemical performance has been demonstrated, for example, on Pd/Fe_3O_4.[25]

This certainly incomplete list emphasizes the need for a comprehensive characterization of metal-oxide interactions, which is also required if one seeks insight into catalytic processes taking place on such systems. The careful investigation

of particle growth on oxide supports might be a first step in this direction. Although the number of such experiments is large (almost every metal has been deposited onto every oxide), systematic studies are surprisingly sparse. Notable exceptions are the few and comprehensive review articles for metal growth on bulk MgO(001),[4] TiO$_2$(110),[5,11] and alumina films.[6] The problem of many other studies is their limited comparability, as the metals have been precipitated at different thermodynamic conditions onto differently prepared substrates. Moreover, the characterization of the pristine support has not always been performed with the required accuracy. However, only from careful experiments that are liberated from spurious preparation effects, can the kernel of metal-oxide interactions be extracted.

In this combined scanning tunneling microscopy (STM) and photoelectron diffraction (PED) study, we have analyzed the growth of simple (Mg,Ca), transition (Ni,Fe), and noble (Ag,Au) metals on MgO thin films grown on a Mo(001) surface. All experiments have been carried out under identical preparation conditions, guaranteeing a reproducible quality of the MgO surface. The results obtained for the different materials are thus comparable to each other, enabling us to identify decisive growth parameters for metals on oxide supports.

II. EXPERIMENT

The experiments have been performed in two ultrahigh vacuum chambers ($p < 2 \times 10^{-10}$ mbar), both equipped with standard tools for sample preparation and analysis. The first chamber contains a nonmonochromatic x-ray Al $K\alpha$ source, a hemispherical mirror analyzer, and a room-temperature STM and was mainly used to perform the photoelectron-diffraction measurements. The second chamber is equipped with a Beetle-type STM operated at liquid nitrogen temperature and was used to produce the real-space data for the adsystems. Thin MgO films grown on Mo(001) were taken as support for the metal particles.[26,27] The oxide was prepared by reactive Mg deposition at 300 K onto a sputtered and flashed Mo(001) surface at 5×10^{-7} mbar O$_2$ partial pressure. After deposition, the films were annealed to 1100 K for 10 min to stimulate crystallization. The MgO films used in this study were 10–12 monolayer (ML) thick. In this thickness regime, MgO forms atomically flat terraces that are a few hundred nm^2 in size and delimited by [100]-oriented edge dislocations [Fig. 1(a)]. The latter often emanate from the core of vertical screw dislocations, being anchored at the metal-oxide interface [see the encircled region in Fig. 1(a)]. In addition, a well-ordered dislocation network forms directly at the metal-oxide interface, which has however little influence on the surface properties of the 10-ML-thick films.[27] The different line defects compensate the -5.4% lattice mismatch between the MgO and the Mo support. It should be noted that the dislocation lines are not only structural but also electronic perturbations, as they induce acceptor-type gap states that are able to trap electrons.[28] The six metals explored in this study were dosed from either an electron-beam evaporator (Mg, Ca, Ni, Au, and Ag) or an effusive cell (Fe) onto the oxide film held at room temperature. The deposition rates were kept at 0.5 ML/min for all metals.
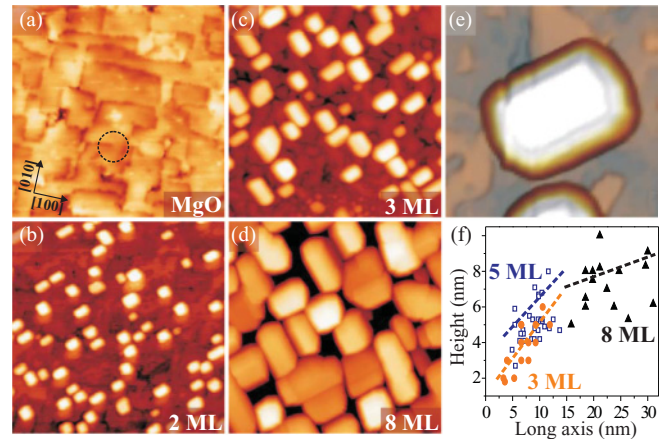

FIG. 1. (Color online) (a) STM image of a 10-ML-thick MgO film grown on Mo(001) (75×75 nm^2, $U_s = 3.5$ V). The dark lines are misfit dislocations that often emanate from screw cores (see circle). (b)–(d) Same film after deposition of increasing amounts of Mg (100×100 nm^2, $U_s = 5$ V). (e) Enlarged image of a characteristic Mg particle on the MgO surface (10×10 nm^2). Note the identical orientation of the MgO film in all panels of this and the following figures. (f) Statistical evaluation of the heights and shapes of Mg particles for different metal exposures. Dashed lines are linear fits of the data, being used to deduce the aspect ratio of the deposits.

III. RESULTS AND DISCUSSION

A. Simple metals: Mg and Ca

Simple metals in general are characterized by a vigorous interaction with oxygen, a fact that is reflected in their large heats of oxidation of more than -500 kJ/mol.[29] The interfacial interaction with MgO(001) is thus expected to be strong, a statement that has been tested in this study with the two alkali-earth metals, Mg and Ca. Similar experiments have also been performed with Li and can be found in the literature.[30,31] In agreement with the anticipated strong metal-oxide coupling, Mg and Ca develop faceted adparticles that reproduce the symmetry of the MgO lattice. The nucleation of Mg sets in at the MgO dislocation lines, where ultrasmall aggregates become discernible in the STM above 1 ML metal exposure [Fig. 1(b)]. A smaller coverage does not lead to particle formation, because the first Mg atoms are incorporated into the MgO lattice.[32] With increasing exposure, rectangular deposits appear in the STM [Fig. 1(c)]. The particle axes thereby align with the orthogonal MgO[110] directions, which are the directions of close-packed O rows in the MgO surface. Most of the particle top facets are atomically flat and single Mg step edges are revealed in the STM, although also roof-shaped deposits can be found. Whereas at small exposure (2 ML), the particles exhibit height-to-width (aspect) ratios of 0.5, they develop pronounced three-dimensional (3D) shapes with aspect ratios of 1 at higher coverage.[33] Above 8 ML exposure, the growth reaches the coalescence regime and neighboring particles merge into a compact film [Fig. 1(d)]. However, open MgO patches remain discernible between the adclusters even for 10 ML nominal Mg coverage.

Although the cluster shapes observed in STM already enable first conclusions on the Mg-MgO interfacial registry, PED measurements have been carried out in addition using the
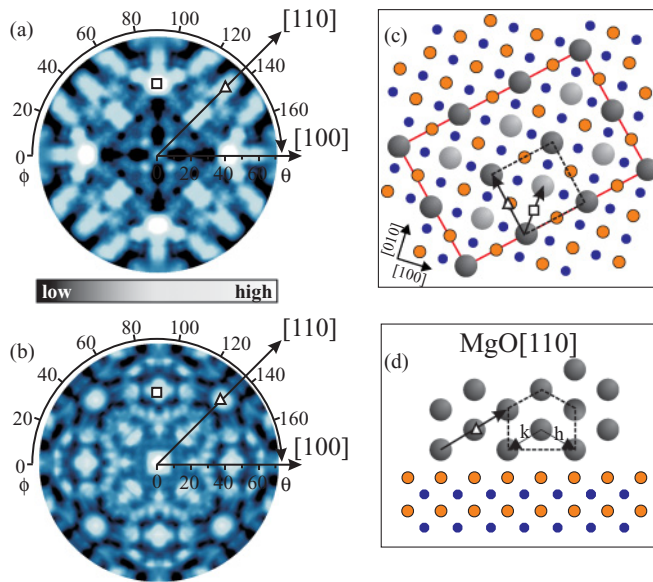
FIG. 2. (Color online) (a) Photoelectron diffraction (PED) stereogram of a Mg cluster film of 10 ML nominal thickness deposited on 10 ML MgO/Mo(001). The plot was taken at the Mg *KLL* Auger line at 1187 eV kinetic energy. (b) Simulation of the PED pattern using the MSCD package (Ref. 34). Main maxima are marked by squares and triangles in both plots and are explained in (c) and (d). Structure model of the ($11\bar{2}0$) hcp Mg plane that serves as interface to the oxide surface: (c) top and (d) side view along the MgO[110] direction. Mg atoms that need to be displaced to sit above an O atom are shown in gray. The Mg unit cell and the particle orientation are marked by a dashed square and a solid rectangle, respectively.

Mg^0 *KKL* Auger transition at $E_{\mathrm{kin}} = 1187$ eV. This particular line has been selected, because the Mg^0 signal of the metal can be easily distinguished from the Mg^{2+} signal of the oxide at 1182 eV. The diffraction data were acquired on Mg cluster films of 10 ML nominal thickness grown on top of a 10-ML-thick MgO film. To obtain a stereogram, the sample was rotated below the analyzer in the range $0° < \phi < 90°$ azimuth angle and $0° < \theta < 70°$ polar angle. Here, the polar angle indicates the tilting against the surface normal [Fig. 2(a)]. The experimental PED plots have been modeled with the MSCD (multiple scattering calculation of diffraction) package which considers single- and multiple-scattering events [Fig. 2(b)].[34]

From both the topographic and diffraction data, a structure model for the Mg-MgO interface is developed [Figs. 2(c) and 2(d)]. The Mg contact plane is identified as the ($11\bar{2}0$) facet of the hcp magnesium, whereby the Mg[0001] axis runs parallel to MgO[110]. This Mg-atom arrangement not only reproduces the square symmetry of the MgO(001), but permits a commensurate relationship with the O lattice of the oxide surface. To reach interfacial registry, the in-plane lattice parameter of Mg needs, however, to be expanded by 12% along Mg[0001] and by 6% along the [$\bar{1}100$] direction. This asymmetric lattice strain is responsible for the rectangular particle shapes, as the cluster growth mainly takes place along the low-strain [$\bar{1}100$] direction. The proposed growth model accounts for two universal stability criteria of metal clusters on the MgO surface and has been observed for other hcp-on-cubic systems before.[35] First, the number of metal-oxygen bonds is

maximized by realizing commensurability between the Mg and the oxide surface. For the hcp ($11\bar{2}0$) configuration, every interfacial Mg atom binds to a lattice oxygen and only one atom per unit cell needs to be slightly displaced from its original position for this [see gray circles in Fig. 2(c)]. Second, the distortion of the particle lattice necessary to reach interfacial registry needs to be minimized. In this regard, Mg is not a good example, as the 6% and 12% mismatches with respect to the bulk Mg lattice are relatively large. The metal nonetheless adopts this unfavorable structure, simply because no other square-shaped interface planes with matching atomic dimensions can be constructed. It should be noted that such a large lattice distortion is only feasible in spatially confined nanoparticles and might even lead to a misfit-induced constraint in the Mg growth. Indeed, the particle width that corresponds to the high-strain [0001] axis never exceeded 5–6 nm in the STM images. In contrast, the vertical growth is strongly promoted by the in-plane lattice strain, giving rise to large aspect ratios for the Mg particles on the MgO surface.

The Mg($11\bar{2}0$) interface model is also consistent with the PED data and allows us to assign the main features in the diffraction stereogram [Fig. 2(a)]. The four equivalent maxima along MgO[100] at $\theta = 43°$ originate from a forward scattering of electrons along dense-packed Mg atom chains with [$3\bar{1}21$] orientation (marked by square symbols in Fig. 2). Those features are reproduced at almost identical polar angles in the simulated stereogram [Fig. 2(b)]. The slightly fainter maxima along the MgO[110] at $\theta = 55°$ are due to scattering along [$10\bar{1}0$]-oriented atomic chains of hcp Mg (triangular symbols in Fig. 2). These peaks also are discernible in the simulation, supporting our Mg($11\bar{2}0$) growth model. A noticeable difference between theory and experiment is the appearance of the central spot that seems to be split into four [110]-oriented maxima in the measurement. Such a splitting is indicative of the presence of Mg atom-chains that are tilted against the surface normal, for instance due to a mosaicity of the particle. Such phenomena are not included in the simulation and could explain the difference from the experimental data. From the measured polar angles, the out-of-plane lattice parameter of the Mg deposits can be approximated by assuming interfacial registry with MgO(001). The derived interlayer separation of 2.0 Å is larger than the bulk Mg value of 1.6 Å, indicating a substantial tetragonal distortion of the Mg lattice in response to the geometric constraints caused by the square MgO lattice.

Calcium, being the second simple metal studied here, is rather similar to Mg from a chemical point of view, but has a 19% larger lattice constant and an fcc bulk structure. At low exposure, Ca also forms rectangular particles on the MgO(001) surface [Fig. 3(a)]. However, the particle edges are rotated by 45° with respect to the Mg boundaries and consequently align with the mixed Mg-O rows running along MgO[100]. The aspect ratio of Ca deposits evolves from 0.4 at low coverage to 0.6 just below the coalescence regime and is therefore smaller than for Mg. Furthermore, large particles develop more irregular shapes and their initially flat top facets become hemispherical [Fig. 3(b)]. Apparently, the Ca growth is governed by interfacial interactions mainly in the initial stage, while larger deposits adopt their own morphology. Also the nucleation densities of Ca and Mg differ substantially.
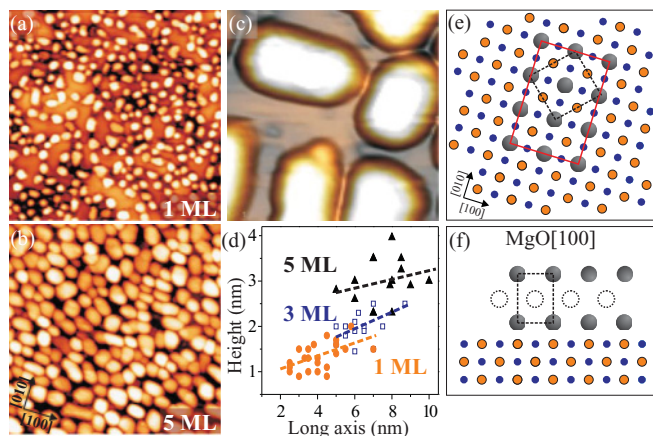
FIG. 3. (Color online) (a), (b) STM images of 10 ML MgO/Mo(001) taken after the indicated Ca exposure ($U_s = 5$ V, 100×100 nm^2). (c) Close-up image of a few Ca particles with characteristic shapes (10×10 nm^2). (d) Statistical evaluation of the structural properties of Ca particles for different metal exposures. Structure model of a (001) plane of fcc Ca on the MgO surface: (e) top and (f) side view along the MgO[100] direction. The fcc Ca unit cell is marked by dashed lines; the particle edges are depicted by a red, solid rectangle. Filled and broken circles in (f) indicate atoms in the plane of view and the next plane, respectively.

Whereas Ca particles grow with an average number density of 25×10^{11} deposits per cm^2 at 300 K, this value decreases to 6.8×10^{11} cm^{-2} for Mg.

The interfacial registry of the Ca-MgO system has been derived only from the STM data and is therefore less reliable than in the Mg case. The observed cluster shape together with the Ca lattice parameter renders the (001) facet of fcc Ca the most probable interface plane [Figs. 3(e) and 3(f)].[30] Hereby, the dense-packed Ca[110] rows run parallel to the MgO[100] direction, fixing the orientation of the particle [Fig. 3(c)]. This binding geometry fulfils the two growth conditions discussed before, as each interfacial Ca is able to bind to a lattice O atom and the required lattice expansion of 5.8% is even smaller than for the Mg-MgO system. It should be noted that hexagonal Ca clusters are also observed in the STM.[36] The associated (111) top facets might be stabilized with respect to the (001) by the low free energy of this surface; however, the number of Ca atoms sitting on top of a lattice oxygen is substantially smaller. Nonetheless, a (111) growth mode might prevail especially for larger Ca deposits, because the structural constraint imposed by the square MgO symmetry is lifted in this case.

B. Transition metals: Ni and Fe

The next group of metals considered here are the transition metals. They also show a high affinity toward oxygen, although typical heats of oxidation are a factor of 3 smaller than for simple metals and display a large spread across the periodic table.[29] The latter phenomenon reflects the influence of the metal d states, more precisely of their energy, symmetry, and electron filling, on the reactivity. Being aware of the arbitrariness of our selection, we have chosen Ni and Fe in this study. Ni is a model system for an electron-rich d^8 material with a large intrinsic lattice mismatch with respect to MgO
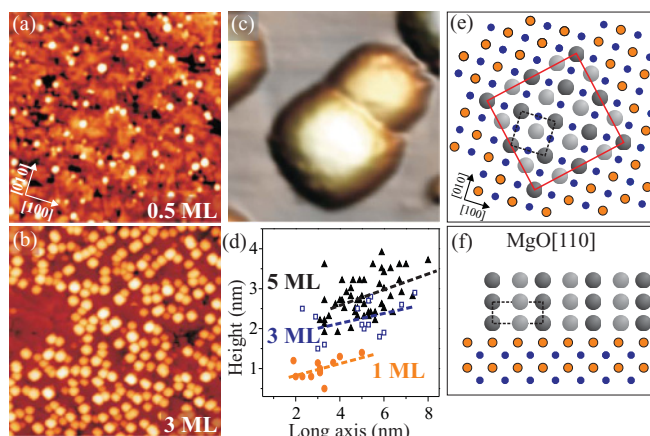

FIG. 4. (Color online) (a), (b) STM images of 10 ML MgO/Mo(001) for two different Ni exposures ($U_s = 3$ V, 100×100 nm^2). (c) Enlarged image of two characteristic Ni particles (10×10 nm^2). (d) Statistical evaluation of the size and shape of Ni particles for different exposures. Structure model of the ($11\bar{2}0$) plane of hcp Ni on the MgO surface: (e) top and (f) side view along the indicated crystallographic direction. Other notations as in Fig. 2.

(-16%), while Fe has d^6 configuration and a lattice parameter that is comparable to that of the oxide (-3.5%).

The STM images in Fig. 4 display two different growth stages of Ni on MgO(001). At low exposure, roughly spherical Ni aggregates containing only a few dozens of atoms form along the dislocation network. With increasing coverage, those clusters develop distinct rectangular and square shapes with edges running along the MgO[110] directions [Fig. 4(b)]. The relationship to the dislocation network remains visible also in this stage, as clusters seem to arrange in chainlike configurations. With increasing Ni coverage, the particles become strictly 3D-like with aspect ratios evolving from 0.25 to 0.5. The coalescence regime for Ni is reached at a nominal coverage of $\sim$5 ML and accompanied by a flattening of the deposits due to merging with their neighbors.

To establish an interface model, PED measurements have been performed on these Ni particle ensembles, using the Ni $2p$ core level at $E_{\rm kin} = 634$ eV (Fig. 5). The diffraction pattern is not as clear as in the Mg stereogram, most likely due to a larger spread in cluster orientations and shapes. Intensity oscillations are discernible along the four equivalent MgO[100] directions
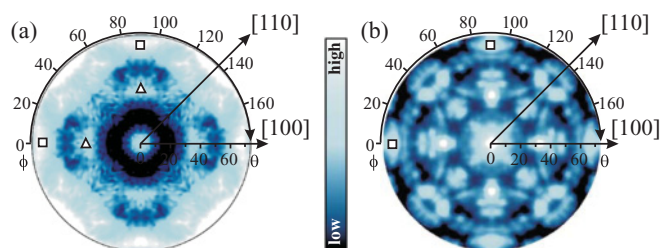

FIG. 5. (Color online) Experimental (a) and simulated (b) photo-electron diffraction stereogram of a Ni cluster film of 7 ML nominal thickness grown on 10 ML MgO/Mo(001). The data are taken at the Ni $2p$ core level ($E_{\rm kin} = 1187$ eV). The most prominent features are the four maxima along the MgO[100] direction that are indicated by the square.

at $\theta = 62°$, indicating a square symmetry of the Ni contact plane [square symbols in Fig. 5(a)]. Four additional maxima can be identified at $\theta = 35°$, as marked by triangles. The intensity course along the MgO[110] is nearly featureless. A first attempt to simulate the PED stereogram with a Ni fcc cluster exposing a (001) interface plane could not reproduce the experimental findings. This disagreement is not surprising, as 16% expansion of the fcc Ni lattice would be necessary to reach commensurability with MgO(001).[37] We have therefore considered a Ni hcp model, where the $(11\bar{2}0)$ plane serves as interface and the [0001] direction runs parallel to the [100] direction of the oxide surface [Figs. 4(e) and 4(f)]. In this geometry, commensurability with the MgO is achieved and every interfacial Ni atom is able to bind to a surface oxygen. Moreover, the required distortion of the Ni lattice is reduced to +4% and −2% along the hcp [0001] and [1100] directions, respectively. From the PED maxima at $\theta = 62°$ along MgO[100], the out-of-plane lattice parameter of hcp Ni is approximated as 1.1 Å, being close to the interlayer spacing in an ideal hexagonal structure (1.24 Å).

The PED simulation of a $(11\bar{2}0)$-oriented hcp particle is able to reproduce the main features of the experimental stereogram [Fig. 5(b)], although the agreement is not as good as in the Mg case. A probable explanation for the underlying morphological and rotational disorder of the Ni deposits is their hexagonal crystal structure, which is unusual for this fcc metal. However, other experimental and density functional theory (DFT) studies also reported the growth of Ni hcp nanodots, which is an effective means to reduce the lattice mismatch with the MgO support.[38,39] Only for clusters above ∼4.5 nm diameter does the fcc motif become energetically favorable. The associated transition from hcp to fcc Ni might be another reason for the blurred PED pattern observed here. Once again, the structural deviation between small deposits and bulk Ni emphasizes the importance of good interfacial registry for particle growth on the MgO surface.

For iron as the second transition metal in this study interfacial interactions are relevant as well (Fig. 6). Whereas at low coverage, the geometry of the aggregates is difficult to assign, larger particles develop pronounced square shapes. The particle edges hereby align with the MgO[110] direction, as observed for Ni before. The mean aspect ratio increases from 0.5 at low to 0.7 at intermediate coverage. Surprisingly, the particle density of Fe of 29×10^{11} cm^{-2} is almost three times larger than for Ni (12×10^{11} cm^{-2}). Only in the initial growth stage does Fe nucleate at the MgO dislocation lines, while at higher coverage particles form also on the terraces. At certain preparation conditions, ordering effects of Fe can be observed on the MgO surface, the origin of which will be discussed in a forthcoming presentation.

Thanks to the perfect lattice match between bcc Fe and MgO(001), the interfacial registry is readily deduced for this system. The contact plane is the (001) facet of bcc iron with its [100] direction running parallel to the [110] direction of MgO [Figs. 6(e) and 6(f)]. This arrangement fulfils all binding motives discussed before. The interfacial Fe atoms sit above the O ions in the surface and the required distortion of the Fe lattice is as small as 3.5%. Similar conclusions were already drawn from earlier Fe growth studies on bulk MgO and MgO/Ag thin films.[40,41]
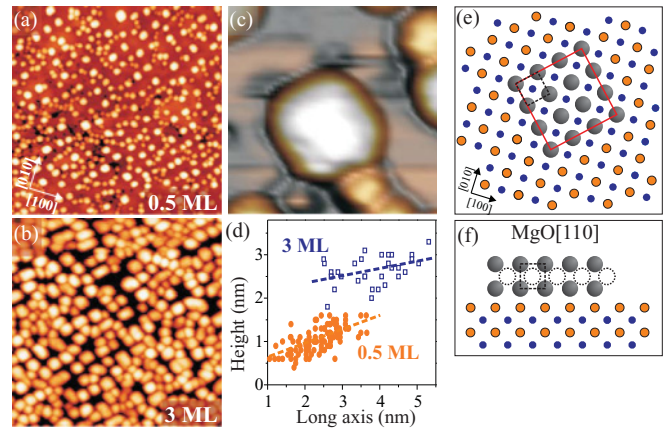

FIG. 6. (Color online) (a), (b) STM images of Fe particles on 10 ML MgO/Mo(001) ($U_s = 4.5$ V, 100×100 nm^2). (c) Image of a characteristic Fe particle (10×10 nm^2). (d) Structural data of Fe deposits obtained for two different metal exposures. Structure model of the (001) plane of bcc Fe on the MgO surface: (e) top and (f) side view along the indicated crystallographic direction. All notations as in Fig. 3

C. Noble metals: Ag and Au

Silver and gold differ from all metals discussed before in their low heats of oxidation, −28 kJ/mol for Ag and −50 kJ/mol for Au.[29] Consequently, the growth of noble metals on the MgO surface is expected to be less affected by metal-oxide interactions, which should lead to the formation of clusters with bulklike lattice parameters and symmetries. Although this expectation is met for Au, it does not hold for Ag as shown in the following.

Silver nucleates again on the MgO dislocation network, whereby mean particle densities of 8×10^{11} cm^{-2} are revealed (Fig. 7). Already in the initial growth stage the perfect lattice match with the MgO support becomes evident. The clusters develop pronounced square shapes with edges aligned with the orthogonal MgO[110] directions. Silver shows a large tendency for 3D growth. While the initial aspect ratio is around 0.5, it quickly rises to 1 at higher coverage. In this stage, the Ag particles can be considered as almost ideal nanocubes, characterized by square bottom and top planes and nearly perpendicular side facets. This geometric peculiarity becomes even more pronounced when the sample is annealed to 550 K [Fig. 7(a)]. The interfacial registry between Ag and the MgO support is readily deduced from the observed particle shapes and has been addressed in various papers before.[42,43,47] The Ag clusters form fcc (001) interface planes, whereby the Ag[100] aligns with the MgO[100] direction [Figs. 7(e) and 7(f)]. In this way, interfacial Ag atoms exclusively bind to lattice oxygen, which requires 3% expansion of the Ag bulk lattice only. The development of well-defined particle shapes can thus be understood despite the exceptionally low affinity of silver toward oxygen.[29]

Gold reproduces several Ag properties, e.g., the chemical inertness and the lattice parameter; however, its growth characteristic on the MgO(001) is nearly antipodal to that of silver. Already at lowest coverage, the Au atoms assemble into hexagonal and triangular deposits, with the nucleation starting
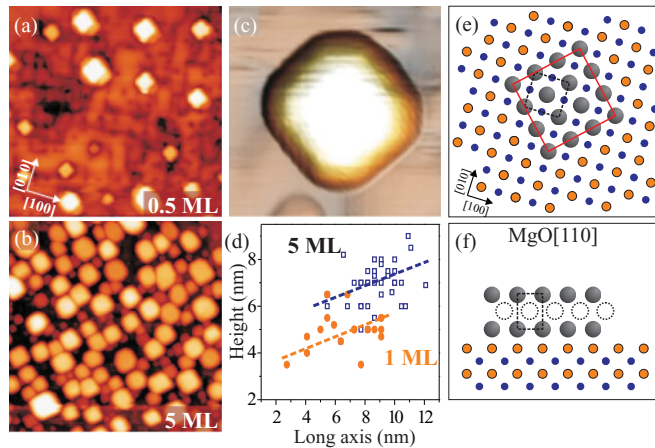
FIG. 7. (Color online) (a), (b) STM images of 10 ML MgO/Mo(001) for two different exposures of Ag (U_s = 4.5 V, 100 × 100 nm^2). For image (a), the sample has been slightly annealed to 550 K after Ag deposition. (c) Close-up image of a characteristic Ag particle (10 × 10 nm^2). (d) Statistical evaluation of the geometry of Ag particles for two metal exposures. Structure model of the (001) plane of fcc Ag on the MgO surface: (e) top and (f) side view along the indicated crystallographic direction. All notations as in Fig. 3.

again along the dislocation network. With increasing coverage, the threefold particle symmetry becomes more and more evident in the STM images, in contrast to the fourfold nature of the support (Fig. 8). Apparently, the Au-MgO coupling is insufficient to fix the shape of the adparticles. However, also Au deposits are not randomly oriented on the surface, as one of the particle edges always aligns with a MgO[110] direction. The Au clusters have the lowest aspect ratio of all studied metals, evolving from 0.2 at submonolayer coverage to 0.3 at around 2 ML. The particle top facets are usually atomically
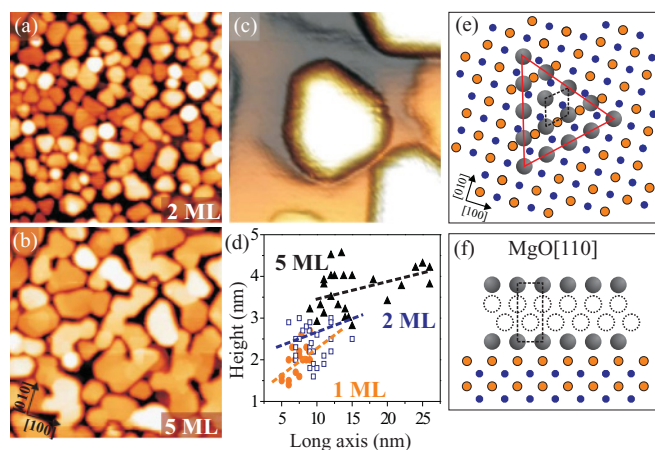

FIG. 8. (Color online) (a),(b) STM images of 10 ML MgO/Mo(001) after dosing with two different amounts of Au (U_s = 5 V, 100 × 100 nm^2). (c) Close-up image of a characteristic Au particle (10 × 10 nm^2). (d) Statistical evaluation of the size and shape of Au particles for different exposures. Structure model of the (111) plane of fcc-Au on the MgO surface: (e) top and (f) side view along the indicated crystallographic direction. All notations as in Fig. 3.

flat. Due to the low aspect ratio of the deposits, the coalescence regime for Au is already reached at 2.5 ML nominal coverage. Au particles grow with typical densities of 15×10^{11} cm^{-2} on the MgO surface, an intermediate value for the metals explored here.

The hexagonal shape of Au islands immediately suggests the Au[111] to be the preferential growth direction [Figs. 8(e) and 8(f)]. In this case, only one of the three equivalent Au axes is commensurate with the MgO[110], while no defined registry is realized for the other two. In the direction parallel to MgO[110], Au atoms occupy top sites of the O sublattice, which requires a lattice distortion of −3%. Apparently, already this uni-directional interaction is sufficient to orient the whole adparticle on the MgO support. The fact that Au islands develop hexagonal shapes and do not mimic the square symmetry of the oxide lattice is compatible with the relatively small Au affinity toward oxygen and the low free energy of the Au(111) surface.

D. Discussion

In the previous sections, we have provided detailed information on the growth characteristic and interfacial registry of various metal particles on the MgO(001) surface. With the exception of Au, all particles exhibit a twofold symmetry, indicating pronounced interfacial coupling to the square-shaped oxide support. An obvious explanation for such particle shapes is the formation of metal-oxygen bonds across the interface, which was indeed identified as the dominant contribution to the metal-oxide adhesion.[9,10,44,45] The calculated binding strength of single adatoms to regular O sites in the MgO surface ranges from 0.4 and 0.8 eV for Ag and Au,[9] to more than 1.0 and 2.0 eV for various simple[30] and transition metals[44,46] (Pd, Ni, Pt), respectively. The strong adsorption of transition metals is owed to an effective mixing of their partly filled d shells with the O $2p$ orbitals. In contrast, the binding to cationic sites in the MgO surface is significantly smaller and hence less important for the total metal-oxide adhesion. For example, the $Pd - Mg_{MgO}$ bond (0.52 eV) is almost three times weaker than the $Pd - O_{MgO}$ bond (1.44 eV).[46,47] It should be noted that adsorption energies might be considerably higher when the bulk MgO is replaced with an ultrathin film supported by a metal substrate.[15,45] In this case, charge transfer processes through the oxide film may become active, initiating effective electrostatic and polaronic interaction schemes. However, for the 10-ML-thick MgO films used here, the thin-film contribution to the adhesion has already died down considerably. The simple interaction picture sketched above will also change in the presence of oxide defects, as discussed later in the paper.

The strength of the metal-oxygen bond is however not the only parameter that governs the growth of adparticles on the MgO surface.[17–19] Other factors that determine the cluster adhesion E_{adh} are the surface free energies of the metal particle γ_{metal} and the oxide surface γ_{oxide}, as reflected in the universal growth formula[7]

$$E_{adh} = \gamma_{metal} + \gamma_{oxide} - \gamma_{interface}. \quad (1)$$

The term $\gamma_{interface}$ describes the effect of interfacial bond formation, as discussed before. It has been derived from

TABLE I. Structural parameters and energies that determine the growth of metal particles on the MgO(001) surface. For rectangular interface structures (Mg and Ni), the parameters for the nonequivalent directions are reported separately. See text for details.

Metal	MgO-metal adhesion $\gamma_{interface}$		Surface free energy γ_{metal} (J/m^2) (Ref. 49)	Interface adhesion E_{adh} (J/m^2)	Young's modulus E (GPa) (Ref. 29)	Lattice mismatch at the interface Δ (%)	Elastic energy E_{elast} (J/m^2)	Net adhesion E_{net} (J/m^2)
	Adatom adsorption energy (kJ/mol)	M-O bonds per MgO unit cell						
hcp Mg								
[0001]	49.2 (Ref. 48)	1	0.64	0.18	45	−12%	0.49	0.67
[1100]						−6%	0.18	0.36
fcc Ca	82.0 (Ref. 30)	1	0.35	−0.42	20	−5.8%	0.08	−0.34
fcc Ni	170.7 (Ref. 46)	2	2.70	−0.52	214	−16%	5.48	5.0
hcp Ni								
[0001]	170.7 (Ref. 46)	2	2.70	−0.52	214	+4%	0.34	−0.18
[1100]						−2%	0.09	−0.43
bcc Fe	136 (Ref. 51)	2	2.66	0.10	197	−3.5%	0.21	0.31
fcc Ag	40.5 (Ref. 46)	2	1.20	0.44	72.5	−2.6%	0.08	0.52
fcc-Au	85.8 (Ref. 46)	1.5	1.60	0.39	74.5	−2.6%	0.08	0.47

DFT calculations of single-atom binding energies to bulk-MgO(001), multiplied by the number of bonds per unit area dA.[46,48] These values only provide an upper bound, as the single-atom interaction is expected to decrease in an atom assembly due to depolarization effects at the interface. Also estimates for γ_{metal} have been taken from the literature.[49] The surface energies are here averages over the most stable cluster facets, a simplification that is justified because energy differences between the facets of one metal are much smaller than between different metals. The term γ_{oxide} is neglected for a qualitative description of the growth behavior, as MgO(001) is used as support throughout the study. The disregard of γ_{oxide} however puts all energies on a relative scale. Based on these approximations, the adhesion of the different clusters is calculated with Eq. (1) (Table I).

The approach presented so far neglects an important contribution to the cluster growth.[50] An attractive interaction via interfacial metal-oxygen bonding only occurs if the particles are able to develop contact planes that are in registry with the oxygen sublattice of the MgO(001). The importance of this geometrical constraint has clearly been shown by our experiments which revealed the formation of a commensurate interface structure even if the contact plane is not a low-energy surface of the respective metal. To render a certain crystallographic cut commensurate with the oxide surface, elastic lattice deformations are required in the bottom layers of the deposits. The associated strain will be released as the particle grows higher, for instance by relaxing the metal-metal bond lengths or inserting dislocation lines. The required energy for the lattice distortion has been approximated from the mismatch Δ between bulk metal and MgO(001) and the Young's modulus E, which is a measure for the elasticity of the ad-metal. The elastic energy $E_{elast} \propto E\Delta^2$ always has a positive sign with respect to the negative (attractive) metal-oxide adhesion and therefore leads to a more positive (smaller) net adhesion of the deposit. It should be noted that the elastic approach completely neglects the possibility of plastic deformations inside the particle, for instance by inserting dislocation lines and stacking faults directly at the interface.

The inclusion of these more sophisticated growth phenomena is beyond the scope of this paper.

The net adhesion E_{net}, being the sum of the attractive metal-oxygen interaction and the repulsive distortion energy, now determines the equilibrium shape of the metal deposits. While a more positive E_{net} (less attractive interaction) results in prolate, 3D-like particles with small contact planes, a more negative (attractive) value renders the particles flatter. As the particle shape is an observable quantity, the interplay between interfacial adhesion and elastic distortion can be tested with the help of our STM data.

Figure 9(a) displays a plot of the net adhesion together with the measured aspect ratios for all adparticles investigated on the MgO(001) surface. In spite of the crudeness of our model, aspect ratio and net adhesion are clearly correlated for most of the metals. Mg and Ag, for example, develop relatively tall clusters, reflecting the weak interfacial metal-oxide interaction. For Mg, this trend is further enhanced by the large lattice distortion that is required to obtain a commensurate interface plane. Calcium, on the other hand, forms oblate clusters. The different growth behavior is readily attributed to the enhanced Ca-MgO adsorption strength and the high elasticity of Ca, both promoting the development of a commensurate interface. Our model also provides an energetic argument against the formation of Ni fcc(001) interface structures, although they would be of square symmetry. The fcc(001) plane needs to be expanded by 16% to reach commensurability with the MgO, which drastically increases E_{elast} and makes the net adhesion highly positive [consider the break in the energy scale on Fig. 9(a)]. On the other hand, a hcp(11$\bar{2}$0) contact plane reproduces the experimental data for the Ni clusters with good accuracy.

An interesting exception is gold, which is the only material that develops no commensurate interface with the MgO(001) surface. The small Au-O bond strength in conjunction with a relatively large surface free energy of gold would clearly favor the formation of 3D particles. In contrast, the Au deposits have the lowest aspect ratio of all investigated metals and exhibit a large tendency to wet the oxide film (Fig. 8). This
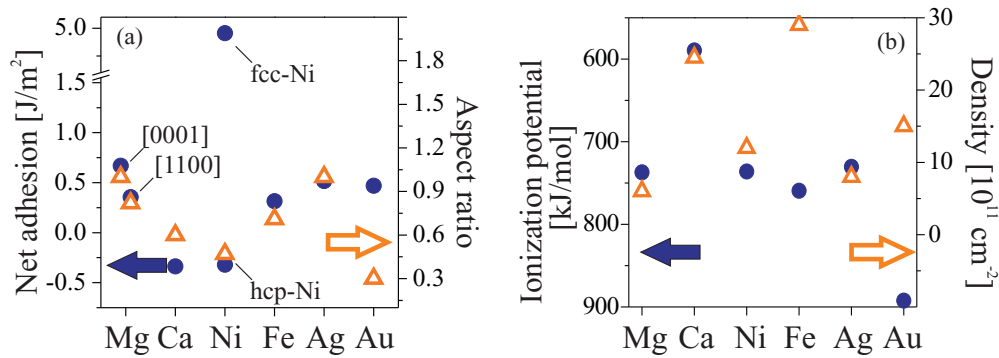
FIG. 9. (Color online) (a) Net adhesion (circles) between the indicated metal and an ideal MgO(001) surface, as calculated with the model described in the text. Apart from Au, the interfacial interaction correlates well with the mean aspect ratio of the deposits (triangles) as deduced from STM topographic images. (b) Comparison between the ionization potential (circles) and the particle density obtained after room temperature deposition of the indicated metals on MgO/Mo(001) (triangles). Again, the correlation is evident with the exception of gold and iron. See text for details.

apparent contradiction has already been the subject of various experimental and theoretical studies, and has been related to the high electronegativity of gold.[15,45,52] As a consequence, anionic Au species were found to develop on ultrathin MgO films via electron tunneling from the Mo support, whereas strong polarization of the oxide charges toward the gold takes place on thicker films.[53] In both cases, the charge displacement opens effective electrostatic and polaronic binding mechanisms between Au and the oxide surface. This charge-mediated interaction is essentially independent of the interfacial registry, which explains why Au grows with its preferred (111) orientation despite the symmetry mismatch with the MgO. In fact, the calculated Au binding energies on thin MgO films are almost degenerate for O top, Mg top, and hollow adsorption sites.[15] The flat Au islands observed in our study therefore indicate a residual influence of the Mo substrate even through 10 ML of MgO, explaining the failure of our simple growth model for gold.

In the final section, we want to address the different nucleation behavior of metals on the MgO/Mo film. According to statistically relevant STM data, the maximum cluster density gradually increases in the order Mg < Ag < Ni < Au < Ca (Table II). Given the high concentration of defects in the MgO surface, particle nucleation needs to be considered as an inhomogeneous process. Typical nucleation parameters, e.g., the diffusion length and the flux of incoming atoms,

TABLE II. Ionization potentials and experimental particle densities for different admetals on the MgO/Mo(001) film. The correlation suggests a nucleation mechanism that is triggered by the oxidation of the first adatoms at defect sites in the oxide surface.

Metal	Ionization potential (kJ/mol) (Ref. 29)	Maximum cluster density (cm^{-2})
Mg	737.05	6×10^{11}
Ca	591.37	25×10^{11}
Ni	736.08	12×10^{11}
Fe	759.22	28×10^{11}
Ag	730.29	8×10^{11}
Au	892.37	15×10^{11}

play therefore only a minor role. In fact, the particle density is controlled by the affinity of the admetals to attach to oxide defects and to form a critical nucleus (heterogeneous nucleation).[16] Misfit dislocations are the most abundant defect type in the MgO films and represent not only morphological imperfections but also electronic inhomogeneities. They can be considered as electron traps, which are able to attract electrons from electropositive adsorbates and capture them in attractive pockets of the oxide Madelung potential.[28,54] According to this scenario, metals with low ionization potential might become cationic at the line defects, which in turn enhances the metal-oxide interaction and facilitates the nucleation process.[32] Correspondingly, Ca as the material with the lowest ionization energy, exhibits the highest nucleation density of all metals, while the densities of Mg, Ag, and Ni clusters are comparable and so are the ionization potentials.

Gold forms an exception again. Although its ionization potential is particularly high, the Au cluster density on the MgO surface is relatively large. A possible explanation has already been given in the discussion of the cluster shapes. Gold has the unique property to become anionic on the MgO/Mo film, as the Au 6s affinity level shifts below the Fermi energy and takes up an extra electron. Similar to cationic species, Au$^-$ also features a strong Coulomb interaction with the oxide Madelung potential, which promotes the formation of a critical nucleus for cluster growth. The fact that also Au preferentially nucleates at the MgO dislocation lines indicates a certain electron-donor character of these defects. Indeed, recent scanning tunneling spectroscopy experiments have identified a filled gap state along the line defect that might be involved in charge transfer toward the gold.[28,55]

The only metal that has not been discussed so far is iron. Its experimental nucleation density is much higher than expected from its large ionization potential. Apparently, the nucleation scheme based on the oxidation of admetals at oxide defects does not apply in this case, a fact that becomes evident from the observation of Fe particles even on the oxide terraces. Another interaction mechanism between Fe and MgO has thus to be considered that is active even on the ideal surface. One possibility would be the spontaneous oxidation of Fe, e.g., via electron exchange with the O anions in the

film or the Mo substrate. However, earlier experiments on Fe-MgO interfaces did not support this scenario.[41,56] Further experiments are therefore required to elucidate the difference in the Fe nucleation behavior with respect to other metals.

IV. SUMMARY AND CONCLUSION

The interfacial interactions between various simple, transition, and noble metals and the MgO(001) surface have been studied with PED and STM by analyzing the structure and morphology of the respective adclusters. Most of the metals develop interface planes that are in registry with the MgO lattice, as revealed from the square and rectangular particle shapes. The variety of contact planes that has been identified in this study is surprisingly large and ranges from hcp(11$\bar{2}$0) for Mg and Ni, fcc(001) for Ca and Ag, to bcc(001) for Fe. In some cases, neither the crystal type nor the exposed cluster facets correspond to structures that preferentially develop in the respective bulk materials. This finding sheds light on the decisive role of interfacial interactions even for oxide supports that are considered to be chemically inert. The driving force for the formation of commensurate interface structures is the creation of a dense array of metal-oxygen bonds, which give the largest contribution to the particle-oxide adhesion. The distortion of the particle lattice that is required to achieve commensurability with the oxide surface has been identified as a second important growth parameter. A lattice mismatch as large as 10% seems to be tolerable for spatially confined nanoparticles. However, well-shaped and thermodynamically stable adclusters only develop if the lattice deformation is smaller. The only metal that does not seek for commensurate interface structures is gold, as it possesses charge-mediated interaction schemes that are independent of an epitaxial relationship.

Our work has demonstrated that probing the equilibrium shape and interfacial registry of metal deposits can be an easy approach to elucidate the nature of metal-oxide interactions. The hereby generated knowledge might provide a useful starting point to elucidate the chemical performance of such systems.

*Corresponding author: nilius@fhi-berlin.mpg.de

[1] *Handbook of Heterogeneous Catalysis*, 2nd ed., edited by G. Ertl, H. Knözinger, F. Schueth, and J. Weitkamp (Wiley-VCH, Weinheim, 2008).

[2] I. E. Wachs, Catal. Today **100**, 79 (2005).

[3] T. Risse, S. Shaikhutdinov, N. Nilius, M. Sterrer, and H.-J. Freund, Acc. Chem. Res. **41**, 949 (2008).

[4] C. R. Henry, Surf. Sci. Rep. **31**, 231 (1998); C. T. Campbell, *ibid.* **227**, 1 (1997).

[5] X. Lai, T. P. St Clair, M. Valden, D. W. Goodman, Prog. Surf. Sci. **59**, 25 (1998).

[6] H-J. Freund, Surf. Sci. **500**, 271 (2002).

[7] M. Bäumer, H.-J. Freund, Prog. Surf. Sci. **61**, 127 (1999).

[8] *Elektronenmikroskopie in der Festkörperphysik*, edited by H. Bethge and J. Heydenreich (Springer, Berlin, 1982).

[9] G. Pacchioni, Solid State Sci. **2**, 161 (2000); A. Del Vitto, G. Pacchioni, F. O. Delbecq, and P. Sautet, J. Phys. Chem. B **109**, 8040 (2005).

[10] V. A. Nasluzov, V. V. Rivanenkov, A. B. Gordienko, K. M. Neyman, U. Birkenheuer, and N. Rösch, J. Chem. Phys. **115**, 8157 (2001).

[11] U. Diebold, Surf. Sci. Rep. **48**, 53 (2003).

[12] M. Sterrer, M. Nowicki, M. Heyde, N. Nilius, T. Risse, H.-P. Rust, G. Pacchioni, and H.-J. Freund, J. Phys. Chem. B **110**, 46 (2006).

[13] T. König, G. H. Simon, H.-P. Rust, M. Heyde, and H.-J. Freund, J. Am. Chem. Soc. **131**, 17544 (2009).

[14] N. Nilius, T. M. Wallis, and W. Ho, Phys. Rev. Lett. **90**, 046808 (2003); N. Nilius, V. Ganduglia-Pirovano, V. Bradzova, V. Simic-Milosevic, J. Sauer, and H.-J. Freund, New J. Phys. **11**, 093007 (2009).

[15] G. Pacchioni, L. Giordano, and M. Baistrocchi, Phys. Rev. Lett. **94**, 226104 (2005).

[16] J. A. Venables, G. D. Spiller, and M. Hanbrücken, Rep. Prog. Phys. **47**, 399 (1984).

[17] C. Noguera, *Physics and Chemistry at Oxide Surfaces* (Cambridge University Press, Cambridge, 1996).

[18] G. Wulff, Z. Kristallogr. **34**, 449 (1901).

[19] D. Chatain, J. Rivolleti, and N. Eustathopoulos, J. Chem. Phys. B **83**, 561 (1986); D. Chatain and J. J. Metois, Surf. Sci. **291**, 1 (1993).

[20] J. Libuda and H.-J. Freund, Surf. Sci. Rep. **57**, 157 (2005).

[21] H. Hövel and I. Barke, Prog. Surf. Sci. **81**, 53 (2006).

[22] X. Lin, N. Nilius, H.-J. Freund, M. Walter, P. Frondelius, K. Honkala and H. Häkkinen, Phys. Rev. Lett. **102**, 206801 (2009); N. Nilius, M.V. Ganduglia-Pirovano, V. Brázdová, M. Kulawik, J. Sauer, and H.-J. Freund, *ibid.* **100**, 096802 (2008).

[23] P. Luches, V. Bellini, S. Colonna, L. Di Giustino, F. Manghi, S. Valeri, and F. Boscherini, Phys. Rev. Lett. **96**, 106106 (2006).

[24] S. Valeri, S. Benedetti, and P. Luches, J. Phys. Condens. Matter **19**, 225002 (2007).

[25] T. Schalow, B. Brandt, D. E. Starr, M. Laurin, S. K. Shaikhutdinov, S. Schauermann, J. Libuda, and H.-J. Freund, Angew. Chem. Int. Ed. **45**, 3693 (2006).

[26] Y. D. Kim, J. Stultz, and D. W. Goodman, Surf. Sci. **506**, 228 (2002); M.C. Gallagher, M. S. Fyfield, L. A. Bumm, J. P. Cowin and S. A. Joyce, Thin Solid Films **445**, 90 (2003).

[27] S. Benedetti, H. M. Benia, N. Nilius, S. Valeri, and H.-J. Freund, Chem. Phys. Lett. **430**, 330 (2006); S. Benedetti, P. Torelli, S. Valeri, H. M. Benia, N. Nilius, and G. Renaud, Phys. Rev. B **78**, 195411 (2008).

[28] H.-M. Benia, P. Myrach, A. Gonchar, T. Risse, N. Nilius, and H.-J. Freund, Phys. Rev. B **81**, 241415R (2010).

[29] *CRC Handbook of Chemistry and Physics*, edited by D. R. Lide (CRC Press, Boca Raton, FL, 2010).

[30] J. A. Farmer, C. T. Campbell, L. Xu, and G. Henkelman, J. Am. Chem. Soc. **131**, 3098 (2009).

[31] P. Myrach, N. Nilius, S. V. Levchenko, A. Gonchar, T. Risse, K.-P. Dinse, L. A. Boatner, W. Frandsen, R. Horn, H.-J. Freund, R. Schlögl, and M. Scheffler, ChemCatChem **2**, 854 (2010).

[32] S. Benedetti, N. Nilius, P. Myrach, I. Valenti, H.-J. Freund, and S. Valeri, J. Phys. Chem. C **115**, 3684 (2011).

[33] Due to tip convolution effects, the particle aspect ratios define only lower bounds of the true geometry.

[34] Y. Chen, F. J. Garcia de Abajo, A. Chassé, R. X. Ynzunza, A. P. Kaduwela, M. A. VanHove, and C. S. Fadley, Phys. Rev. B **58**, 13121 (1998).

[35] G. C. Gazzadi and S. Valeri, Europhys. Lett. **45**, 501 (1999).

[36] P. Myrach, N. Nilius, and H.-J. Freund, J. Phys. Chem. C **113**, 18740 (2009).

[37] C. Di Valentin, L. Giordano, G. Pacchioni, and N. Rösch, Surf. Sci. **522**, 175 (2003).

[38] R. Ferrando, G. Rossi, F. Nita, G. Barcaro, and A. Fortunelli, ACS Nano **2**, 1849 (2008).

[39] S. Sao-Joao, S. Giorgio, C. Mottet, J. Goniakowski, and C. R. Henry, Surf. Sci. **600**, L86 (2006).

[40] B. M. Lairson, A. P. Payne, S. Brennan, N. M. Rensing, B. J. Daniels, and B. M. Clemens, J. Appl. Phys. **78**, 4449 (1995); A. di Bona, C. Giovanardi, and S. Valeri, Surf. Sci. **498**, 193 (2002).

[41] P. Luches, S. Benedetti, M. Liberati, F. Boscherini, I. I. Pronin, and S. Valeri, Surf. Sci. **583**, 191 (2005).

[42] R. Ferrando, G. Rossi, A. C. Levi, Z. Kuntova, F. Nita, A. Jelea, C. Mottet, G. Barcaro, A. Fortunelli, and J. Goniakowski, J Chem. Phys. **130**, 174702 (2009).

[43] O. Robach, G. Renaud, and A. Barbier, Phys. Rev. B **60**, 5858 (1999).

[44] G. Pacchioni and N. Rösch, J. Chem. Phys. **104**, 7329 (1996).

[45] D. Ricci, A. Bongiorno, G. Pacchioni, and U. Landman, Phys. Rev. Lett. **97**, 036106 (2006).

[46] S. Sicolo, L. Giordano, and G. Pacchioni, J. Phys. Chem. C **113**, 16694 (2009).

[47] J. Goniakowski and C. Noguera, Interface Sci. **12**, 93 (2004); A. Ouahab, C. Mottet, and J. Goniakowski, Phys. Rev. B **72**, 035421 (2005).

[48] L. N. Kantorovich, A. L. Shluger, P. V. Sushko, J. Günster, P. Stracke, D. W. Goodman, and V. Kempter, Faraday Discuss. **114**, 173 (1999).

[49] H. L. Skriver and N. M. Rosengaard, Phys. Rev. B **46**, 7157 (1992).

[50] E. Bauer and J. H. van der Merwe, Phys. Rev. B **33**, 3657 (1986).

[51] K. M. Neyman, C. Inntam, V. A. Nasluzov, R. Kosarev, and N. Rösch, Appl. Phys. A **78**, 823 (2004).

[52] M. Sterrer, T. Risse, M. Heyde, H.-P. Rust, and H.-J. Freund, Phys. Rev. Lett. **98**, 206103 (2007); M. Sterrer, T. Risse, U. M. Pozzoni, L. Giordano, M. Heyde, H.-P. Rust, G. Pacchioni, and H.-J. Freund, *ibid.* **98**, 096107 (2007).

[53] K. Honkala and H. Häkkinen, J. Phys. Chem. C **111**, 4319 (2007).

[54] K. P. McKenna and A. L. Shluger, Nature Mater. **7**, 859 (2008).

[55] C. Pauly, M. Grob, M. Pezzotta, M. Pratzer, and M. Morgenstern, Phys. Rev. B **81**, 125446 (2010).

[56] P. Luches, P. Torelli, S. Benedetti, E. Ferramola, R. Gotter, and S. Valeri, Surf. Sci. **601**, 3902 (2007).